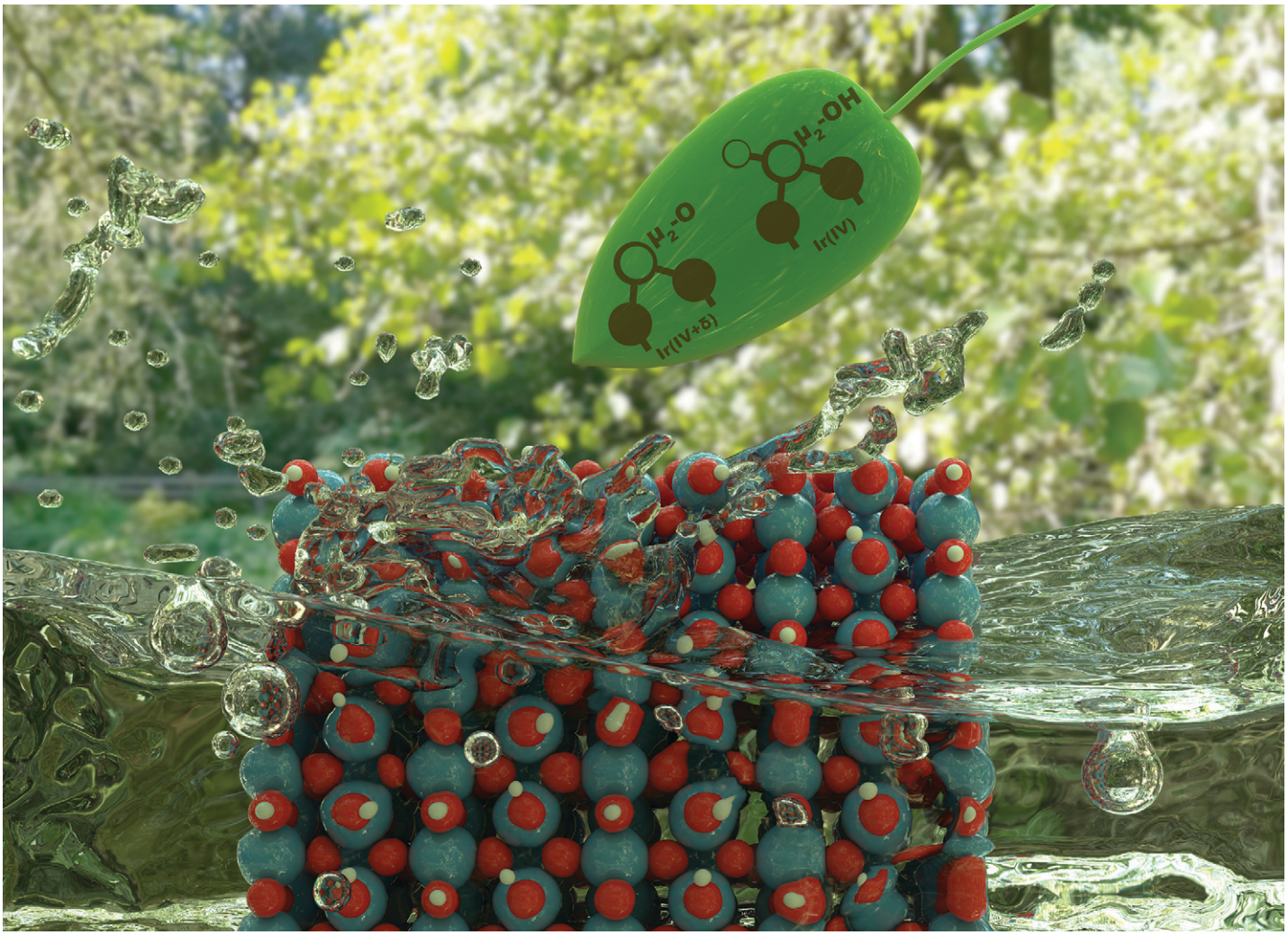

Showcasing research from the inorganic chemistry department of the Fritz-Haber-Institut der Max-Planck-Gesellschaft and Helmholtz-Zentrum Berlin für Materialien und Energie joint group, Catalysis for energy.

Thermal synthesis of electron deficient oxygen species on crystalline IrO_2

Using *ab initio* thermodynamics and *in situ* X-ray photoelectron and absorption spectroscopies we show that the electrophilic O^{I-} that grows on Ir-based oxides under OER forms on $Ir^{IV+\delta}$ by thermal oxidation of rutile-type IrO_2, without the appearance of unstable Ir^{III} species. CO titration experiments confirm the chemical nature of the thermally grown μ_2-O species, showing they have the same spectroscopic and chemical properties associated with the electrophilic O^{I-} species whose coverage is related to OER activity of Ir-based materials. These findings could offer a route to higher-performance stable OER catalysts.

As featured in:

See E. A. Carbonio, T. Jones *et al.*, *Catal. Sci. Technol.*, 2024, **14**, 572.

ROYAL SOCIETY OF CHEMISTRY

rsc.li/catalysis

Registered charity number: 207890

Catalysis Science & Technology

ROYAL SOCIETY OF CHEMISTRY

PAPER

View Article Online
View Journal | View Issue

Cite this: *Catal. Sci. Technol.*, 2024, **14**, 572

Thermal synthesis of electron deficient oxygen species on crystalline IrO_2†

E. A. Carbonio, *[ab] F. Sulzmann,[b] D. Teschner,[bc] J. J. Velasco-Vélez,[bcd] M. Hävecker,[ac] A. Knop Gericke,[bc] R. Schlögl[abc] and T. Jones*[be]

Received 24th July 2023,
Accepted 26th November 2023

DOI: 10.1039/d3cy01026k

rsc.li/catalysis

Water splitting is a promising technology in the path towards complete renewable energy within the hydrogen economy but overcoming the sluggishness of the oxygen evolution reaction (OER) is a major challenge. Iridium-based oxides remain the most attractive materials for the OER under acidic conditions since they offer the combination of activity and stability. Gaining knowledge about how these materials have such an ability is of great interest to develop improved electrocatalysts for the OER. Among the different iridium-based oxides the materials with high concentrations of electron deficient oxygen (O^{I-}) have been shown to have higher OER activity, however, they also have high dissolution rates, seemingly due to the presence or formation of Ir^{III} species. In contrast, rutile-type IrO_2, which does not contain Ir^{III} species, has high dissolution resistance but the OER activity remains comparatively low as only low coverages of O^{I-} species are formed under OER. The apparent link between O^{I-} and Ir^{III} species that comes from these observations has yet to be proven. In this work, using *ab initio* thermodynamics and *in situ* X-ray photoelectron and absorption spectroscopy we show that the same electrophilic O^{I-} species that appear on Ir-based oxides under OER can be formed on $Ir^{IV+\delta}$ by mild thermal oxidation of rutile-type IrO_2, without the presence Ir^{III} species.

Introduction

The oxygen evolution reaction (OER) is a kinetic bottleneck in water electrolysis, requiring high-performance catalysts to achieve low overpotentials. This problem is especially acute for the anodes of proton exchange membrane (PEM) based electrolyzers. An apparent inverse relationship between stability and activity,[1,2] results in only Ir-based materials providing the required combination of stability and activity.[3,4] This has made Ir-based materials the subject of intense scrutiny as highlighted in a number recent review.[5–9] Electrochemical studies of Ir-based catalysts have shown that, while the thermodynamically stable rutile-type IrO_2 shows the higher dissolution resistance,[2,10] hydrated X-ray amorphous oxyhydroxides (IrO_x) show improved activity with respect to their crystalline counterparts at the expense of stability. For instance, a unique oxygen ligand environment facilitates water oxidation in hole-doped $IrNiO_x$ core–shell electrocatalysts.[11–14] The improved activity of amorphous IrO_x was attributed to the presence of electron deficient oxygen, or O^{I-}, based on studies combining X-ray absorption spectroscopy (XAS) at the O K-edge combined with density functional theory calculations (DFT,)[12,15–17] where the O^{I-} species gives a characteristic resonance at *ca.* 529 eV in the O K-edge spectrum. The reduced stability of amorphous materials may be attributable to the presence of Ir^{III} species.[10,18,19] It is then important to understand if there is a link between O^{I-} and Ir^{III}. Unfortunately, the X-ray amorphous nature of IrO_x makes further structural characterization of the observed O^{I-} difficult in XAS studies. And while TEM investigations of amorphous materials have helped to identify key structural features related to activity,[20,21] there is still a pressing need to understand whether there is a difference in active species on amorphous and rutile-type Ir-oxides in order to improve catalyst performance while minimizing stability losses.

The original assignment of O^{I-} in IrO_x to undercoordinated μ_2-O species (O bound to two rather than three Ir-atoms, see Fig. S1†)[12,15,17] has proven to be successful in describing a range of *operando* XAS results at

[a] *Catalysts for Energy, Energy Materials In-situ Laboratory (EMIL), Helmholtz-Zentrum Berlin für Materialien und Energie GmbH, BESSY II, Albert-Einstein-Straße 15, 12489 Berlin, Germany. E-mail: carbonio@fhi-berlin.mpg.de*
[b] *Department of Inorganic Chemistry, Fritz-Haber-Institut der Max-Planck-Gesellschaft, Faradayweg 4-6, 14195 Berlin, Germany. E-mail: tejones@lanl.gov*
[c] *Department of Heterogeneous Reactions, Max Planck Institute for Chemical Energy Conversion, Stiftstraße 34-36, Mülheim an der Ruhr 45470, Germany*
[d] *ALBA Synchrotron Light Source, Cerdanyola del Vallés (Barcelona) 08290, Spain*
[e] *Theoretical Division, Los Alamos National Laboratory, Los Alamos, New Mexico 87545, USA*

† Electronic supplementary information (ESI) available. See DOI: https://doi.org/10.1039/d3cy01026k

both the O K-edge and Ir $L_{2,3}$-edges.[10,11,13,14,18,22–26] This species does not require the presence of Ir^{III}, and could therefore be formed without the deleterious stability effects associated with reduced Ir species. If this assignment is correct, μ_2-O should form on rutile-type IrO_2 under gas-phase conditions; μ_2-O is expected to be stable on rutile-type IrO_2 under vacuum conditions,[27–30] though, to the best of our knowledge, it has not been spectroscopically observed at room temperature or on crystalline powder catalysts.[12,15,17,29,30] Here we address this apparent discrepancy in the assignment of O^{I-} and its possible relationship with Ir^{III} through *in situ* X-ray photoelectron spectroscopy, *in situ* O K-edge XAS, and chemical testing of well-calcined rutile-type IrO_2 combined with DFT calculations. In agreement with its assignment to μ_2-O, we find that the electron deficient-O species can be formed on rutile-type IrO_2 by mild-oxidation (conditions), albeit with a coverage that is less than that observed for IrO_x.

Methodology

Sample preparation

A crystalline rutile IrO_2 (Sigma Aldrich, 99.9%) powder, known to have little OER activity,[15] was calcined at 1073 K for 50 hours under 1 bar O_2 to ensure rutile-type phase purity.[10,16] For some experiments (specified in the figures), an amorphous IrO_x (Alfa Aesar) powder was calcined at 1123 K to ensure crystallization and rutile-type phase purity.[10,16] Characterization of both types of powders before and after calcination has been previously published by our group.[15,16] Unless stated otherwise, (calcined) IrO_2 Sigma Aldrich (99.9%) has been used. For the near ambient pressure (NAP) XPS/XAS measurements, 5 mm diameter pellets where prepared by pressing 50 mg of material under 2 tons for 2 minutes. The samples were placed in a sapphire sample holder between two stainless-steel plates (the front facing plate contained an opening for measurements). Heating was done with an IR laser on the backside stainless-steel plate that was directly in contact with the sample. The sample temperature was measured with a K-type thermocouple placed on top of the sample pellet and held between the sample and the front stainless-steel plate. The temperature was controlled by adjusting the laser power using a PID feedback loop.

For NAP XPS/XAS measurements the samples were kept in UHV, then treated in 0.25 mbar O_2 at 573 K and finally exposed to 0.25 mbar CO. For the CO treatment, the sample was first cooled to 473 K under 0.25 mbar O_2 and then cooled to 313 K under UHV. The sample was then kept in the load lock (base pressure 10^{-7} mbar). The main chamber was filled with 0.25 mbar CO, and after stabilization of the pressure, the load lock valve was open to expose the sample to the 0.25 mbar CO. This methodology has been shown to be a reliable way of testing CO oxidation in the NAP-XPS setup.[17] For all experiments 99.9999% O_2 and 99.97% CO from Westfalen were used.

X-ray absorption and X-ray photoelectron spectroscopy

Measurements were done at the UE56/2-PGM beamline at the BESSY II synchrotron radiation light source in Berlin, Germany (in low alpha mode). The details of the beamline can be found elsewhere.[31]

For the XP difference spectrum, a Shirley background with a 10% offset on the high binding energy side was subtracted from the spectra, which were normalized afterwards. The Ir 4f core-level was measured with a photon energy of 150 eV, which is *ca.* 85–90 eV kinetic energy (KE). This gives an estimated inelastic mean free path (IMPF) of approximately 0.4 nm;[32] note the lattice spacing in the (110) direction is 0.3 nm,[33] making the 150 eV photons surface sensitive. The XA spectra were measured by Auger electron yield (AEY) using electrons at a fixed KE of 514 eV (and pass energy of 50 eV). The probing depth of this measurement is approximately 2–3 nm,[17] or *ca.* 6–10 atomic layers in the (110) direction. XPS and XAS were measured using a Phoibos 150 hemispherical analyzer from SPECS GmbH.

On-line quadrupole mass spectrometry

A quadrupole mass spectrometer (QMS) from Pfeiffer (directly connected to the main reaction XPS/XAS chamber through a leak valve) was used on-line as a means of detecting CO_2 produced from CO oxidation. Ions with m/z = 44, 28, 32, 18 were recorded to follow CO_2, CO, O_2 and H_2O, respectively.

Computational details

Spin polarized density functional theory calculations were performed using the Quantum ESPRESSO package.[34,35] All calculations employed the PBE exchange and correlation potential[36] using PAW datasets from the PSLibrary[37] with a kinetic energy (charge density) cutoff of 60 Ry (600 Ry). Rutile-type IrO_2 surfaces were modeled using 8-layer symmetric slabs with (110) surface termination with the central 4-layer fixed during geometry optimizations. The (110) surface was chosen as it is the lowest energy surface and has been observed to be the dominant facet for rutile IrO_2 subjected to high temperature treatments.[38–40] Since this surface has only in an oxidation state above III, to explore lower oxidation state Ir, we have included surfaces with oxygen vacancies together with bulk heterogenite-type IrOOH and corundum-type Ir_2O_3 (Fig. S7†). Other facets and the effect of Ir vacancies have been previously studied by our group.[10,15,17,18] These do not affect the outcome of this publication. For the surfaces, periodic images were separated by *ca.* 15 Å of vacuum. A k-point mesh equivalent to (6 × 3) for the (1 × 1) surface unit cell was employed with cold smearing using a smearing parameter of 0.01 Ry.[41] For bulk Ir_2O_3 and IrOOH, (6 × 6 × 2) and (8 × 8 × 8) k-point meshes were employed, respectively. O K-edge spectra were computed using the single particle approach implemented in the XSpectra package.[42] Following previous publications,[15] O K-edge spectra were computed in the absence of a core hole. Core level binding energies were computed by the ΔSCF

method[43] using (2 × 4) surfaces, and (2 × 2 × 2) supercells for the bulk structures. These were aligned to experiment using a Δ*SCF* calculation on a (4 × 4 × 4) supercell of bulk rutile-type IrO_2, where the Δ*SCF* shift was aligned to experiment following the procedure outlined in a previous publication.[44] All computed spectra of the surface species were then aligned using this bulk IrO_2 reference. The Ir 4f spectra were computed using a Hopfield model wherein the final state contained an Ir 4f corehole.[18]

The surface phase diagrams were computed by way of *ab initio* atomistic thermodynamics.[45,46] To avoid the well-known over binding of $O_{2,gas}$ predicted by the PBE exchange and correlation potential, the oxygen reference energy was taken from bulk rutile-type IrO_2 as: $E_{O_2} = E_{IrO_2} - E_{Ir} - \Delta H_{f,IrO_2}$, where E_{O_2} is the total energy of O_2, E_{IrO_2} is the computed total energy bulk rutile-type IrO_2; E_{Ir} is the computed total energy of bulk fcc Ir; $\Delta H_{f,IrO_2}$ is the experimental heat of formation of the rutile-type oxide.[47] The enthalpic and entropic corrections for the gas-phase oxygen chemical potential were taken from the NIST JANAF tables,[48] allowing us to express the oxygen chemical potential as: $\mu_{O_2}(T, p_{O_2}) = E_{O_2} + \tilde{\mu}_{O_2}(T, p_0) + k_B T \ln(p_{O_2}/p_0)$, where p_0 is standard pressure. Here, $\tilde{\mu}_{O_2}(T, p_0)$ is the tabulated enthalpic and entropic contributions for gas-phase O_2 at standard pressure. The final term accounts for pressure variations of the ideal-gas reservoir. We assume water will be the major hydrogen source in air or under NAP-XPS conditions, which allows us to write the hydrogen chemical potential as: $\mu_{H_2}(T, p_{O_2}, p_{H_2O}) = \mu_{H_2O}(T, p_{H_2O}) - 1/2\mu_{O_2}(T, p_{O_2})$, where $\mu_{H_2O}(T, p_{H_2O}) = E_{H_2O} + \tilde{\mu}_{H_2O}(T, p_0) + k_B T \ln(p_{H_2O}/p_0)$.[43] In this case, the energy of the gas-phase water molecule, E_{H_2O}, was computed at the *Γ*-point in (20 × 20 × 20) Å^3 box and the enthalpic and entropic contributions, $\tilde{\mu}_{H_2O}(T, p_0)$, were again taken from the NIST JANAF tables. This choice of μ_{H_2} can be seen to be conservative as compared to hydrocarbon sources that may be present in air or under typical NAP-XPS conditions, since the employed definition involves the heat of formation of water. The predicted stability of OH structures is then expected to be a lower bound for what is found experimentally. In all cases the entropic contributions from the adsorbates have been ignored. From previous work we anticipate this will lead to an underestimation of the thermal stability of adsorbed species by about 100–150 K,[44] which will not change the results presented herein.

Results and discussion

Highly electrochemically active amorphous IrO_x contains electron deficient oxygen species, or O^{I-}, assigned to doubly coordinated oxygen atoms (μ_2-O) (see structure in Fig. S1†) that have not been observed on rutile-type IrO_2 powder under UHV[15–17] and are present only in small amounts under OER conditions.[10] It is expected that such species could form under gas-phase oxygen. To test the conditions under which this will occur, we turn to *ab initio* thermodynamics. We find

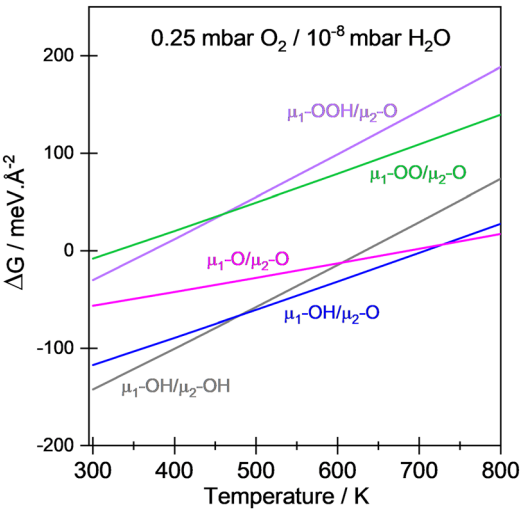

Fig. 1 Calculated surface phase diagram for the surface species on rutile IrO_2 (110) under 0.25 mbar O_2 and 10^{-8} mbar H_2O, where the zero of energy is the bare (110) surface.

that at room temperature rutile-type IrO_2 is predicted to be covered by μ_1-OH/μ_2-OH species (see structures in Fig. S1†) under 0.25 mbar $O_{2,gas}$ even when only trace (10^{-8} mbar) H_2O_{gas} is present (Fig. 1), however, μ_2-O is predicted to form at higher temperatures under these partial pressures due to the entropic cost of hydrogen adsorption. And critically, for the (110) surface terminated IrO_2, these μ_2-O form in the absence of Ir^{III}. This predicted presence of μ_2-O in the absence of Ir^{III} can be tested experimentally by way of NAP-XPS since these are realizably characterized by NAP-XPS.

This finding is consistent with previous publications on IrO_2 thin layers grown on single crystals that have shown that surface species were observed to mainly consist of protonated O (–OH) species, that form rapidly due to background H_2 content, unless the thin film is kept at higher temperatures.[30] Here, unlike the μ_2-OH sites, the μ_1-OH sites are not expected to be oxidized to μ_1-O under mbar gas-phase conditions when trace water (or other H sources) is present (Fig. 1). Under experimentally accessible conditions at mbar O_2 pressures (Fig. 1), the μ_1-O phase is only metastable (below *ca.* 700 K) owing to the strong O–H bond of μ_1-OH. Furthermore, the (hydro)peroxo species argued to participate in OER and postulated as possibly present in IrO_x (ref. 49 and 50) appear at higher energies and are unstable at temperatures above *ca.* 350 K under gas-phase conditions with mbar pressures and should therefore not be observed. Thus, NAP-XPS offers an ideal means of testing the assignment of O^{I-} and its relationship with Ir^{III}. We investigated this experimentally by means of NAP-XPS and XAS.

The Ir 4f spectrum of the IrO_2 pellet (Fig. 2a) shows the typical line shape and binding energy (BE) for rutile-type IrO_2.[15,16,29,30] The O-K edge spectrum of rutile-type IrO_2 (Fig. 2b) shows a sharp resonance at *ca.* 530 eV, characteristic of the lattice μ_3-O.[16,17] Computed Ir 4f and O-K edge spectra for the different species are shown in Fig. 2c and d (and S2†).

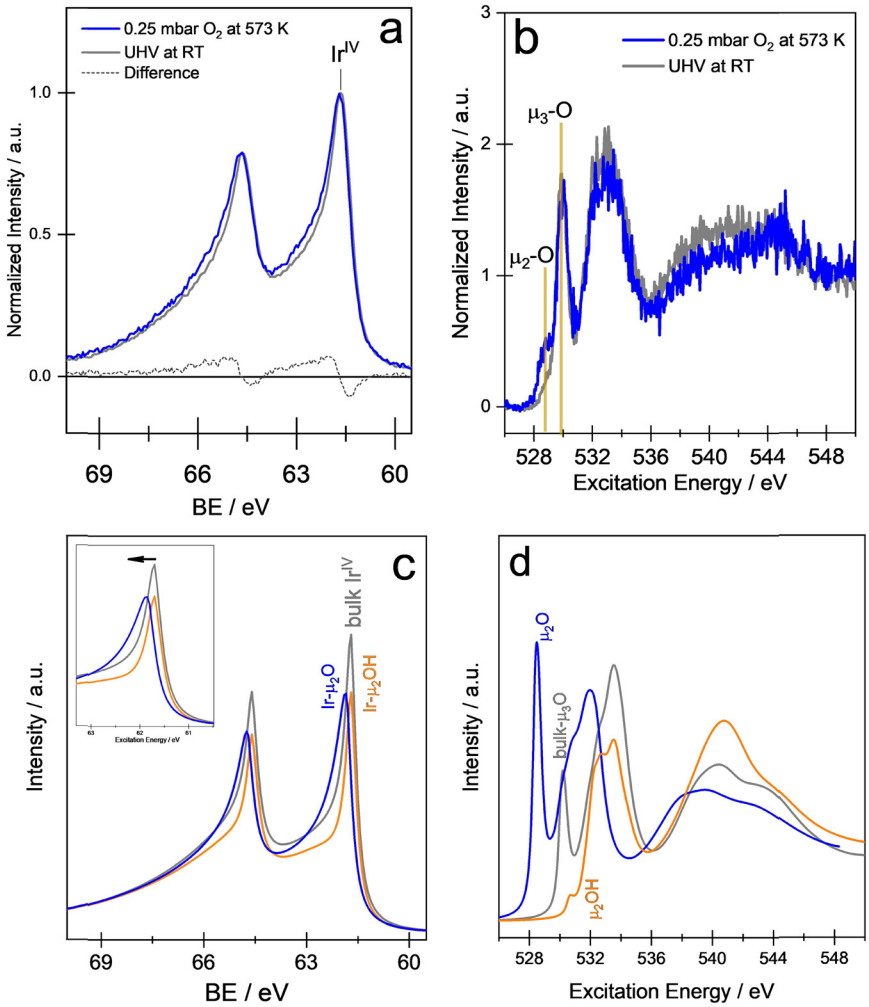

Fig. 2 (a) Ir 4f of rutile IrO_2 in UHV at RT, under 0.25 mbar O_2 at 573 K, and difference spectrum. (b) AEY O K-edge of rutile IrO_2 in UHV at RT and under 0.25 mbar O_2 at 573 K. Vertical lines indicate the corresponding species giving rise to each resonance. (c) Computed Ir 4f spectra for bulk-Ir^{IV} in rutile-type IrO_2, surface Ir–μ_2-OH and surface Ir–μ_2-O. Inset shows a zoom in to the Ir $4f_{7/2}$. (d) Computed O K-edges for μ_3-O (bulk-O), μ_2-OH and μ_2-O species.

As OH species have a very low resonance intensity per atom at the O K-edge,[10,23] the μ_1-OH and μ_2-OH species — which are predicted to cover the surface and have resonances at *ca.* 529.5 and 530.5 eV (Fig. S2†) — will have very low intensity compared to the major bulk contribution of μ_3-O. A clear resonance from μ_1-OH and μ_2-OH species is then not expected, nor is it seen. No resonance at *ca.* 529 eV (characteristic of μ_2-O species on iridium oxides) is observed at room temperature under UHV (see also Fig. S3†), in agreement with our *ab initio* thermodynamics predictions (Fig. 1) and previous findings.[16]

At elevated temperatures the surface phase of the rutile-type oxide is predicted to transform from μ_2-OH to μ_2-O (Fig. 1). From the computed spectra, this phase transition is predicted to introduce a higher binding energy component and additional asymmetry in the Ir 4f spectrum (Fig. 2c), and a *ca.* 529 eV resonance in the O K-edge spectrum (Fig. 2d and S2†). As predicted, the Ir 4f XP spectrum of the rutile-type IrO_2 shows a slight broadening upon heating to 573 K under 0.25 mbar O_2. This broadening can be assigned to the $Ir^{IV+\delta}$ formed upon dehydrogenation of the μ_2-OH sites to form an electron deficient O-species, $O^{(I+\delta)-}$, which also yields $Ir^{IV+\delta}$ due to the covalency of the Ir–O bond (in agreement with earlier observations).[10,23,30] For simplicity, we call this electron deficient O-species O^{I-} throughout this manuscript (as named in the literature).[12,13,15–17,50] The change becomes more apparent when we analyze the difference spectrum (Fig. 2a), which resembles computed spectra for Ir bound to μ_2-O (Fig. 2c). At the O-K edge, a resonance at *ca.* 529 eV can also be seen to develop when heating the sample under O_2 (Fig. 2b, see also S4 and S5†). The species formed by mild thermal oxidation has the same spectroscopic characteristics as the species found in amorphous IrO_x (under UHV) and iridium oxyhydr(oxides) under OER.[10,15–17,23]

The surface phase transition from μ_1-OH/μ_2-OH to μ_1-OH/μ_2-O is also predicted to show changes in the projected density of states (pDOS) on the rutile-type IrO_2 (Fig. 3). The O 2p pDOS (Fig. 3a) shows an increased intensity at *ca.* 0.2, 2

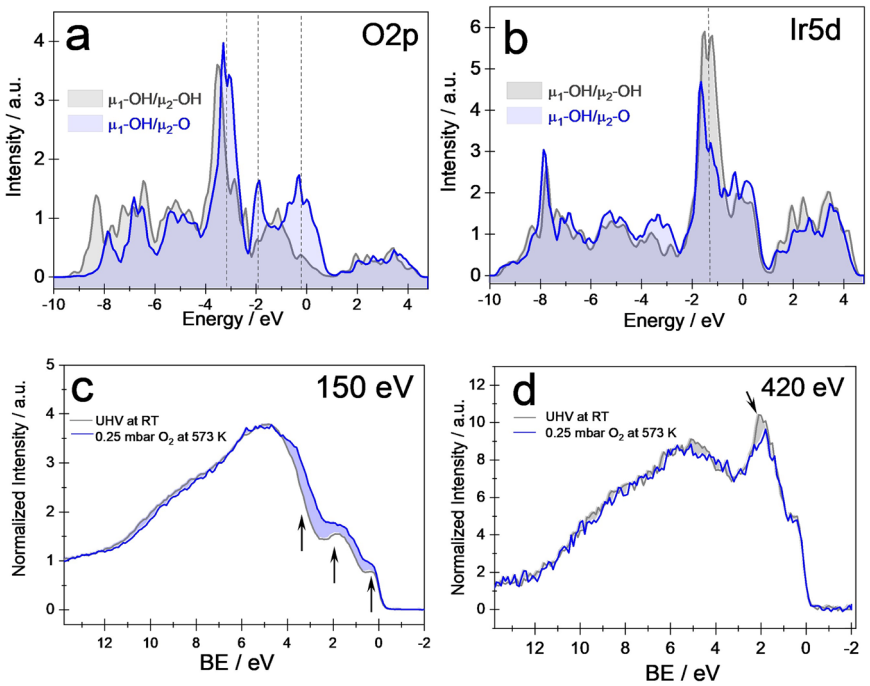

Fig. 3 DOS for O 2p (a) and Ir 5d (b) states for different O surface species on rutile-type IrO_2. VB measured at 150 eV (c) and 420 eV (d) for rutile-type IrO_2 in UHV and RT and under 0.25 mbar O_2 at 573 K.

and 3 eV below the Fermi energy for the surface with μ_2-O species. At the same time, Ir shows a loss of 5d states at about 1.3 eV below the Fermi energy for the Ir–μ_2-O species (Fig. 3b) due to its oxidation. The computed pDOS can be compared to valence band (VB) measurements of the rutile-type IrO_2. These have been taken under UHV and under 0.25 mbar O_2 at 573 K, as shown in Fig. 3c and d, respectively. The VB were measured at two different photon energies, 150 eV and 420 eV. The first one (150 eV) is near the Cooper minimum of iridium, thus maximizing the sensitivity to oxygen species due to the comparatively high O 2p cross-section; the O 2p cross-section is *ca.* 3 times that of the Ir 5d at this energy.[51] For the VB measured at 420 eV the Ir cross section is *ca.* 5 times larger than that of the O 2p, and the spectra are dominated by the Ir 5d contribution.[51] The VB measured at 150 eV under oxygen at 573 K (Fig. 3c) shows an increased intensity between 0–4 eV when compared to the VB measured under UHV at RT. At the same time, the VB measured at 420 eV (Fig. 3d) under oxygen at 573 K shows a slight loss of intensity at *ca.* 1.5 eV when compared to the VB measured under UHV at RT. These changes although small, are reproducible (see Fig. S6†) and consistent with the predicted changes in the pDOS for the phase transition from μ_2-OH to μ_2-O, and agree well with the XPS and XAS results (Fig. 2). Computed O K-edge spectra, pDOS and the calculated BE for bulk Ir^{III} compounds and rutile IrO_2 surfaces containing Ir^{III} and $Ir^{III+\delta}$ (for both μ_1-OH/μ_2-OH and μ_1-OH/μ_2-O surfaces) can be found in the ESI† (see Fig. S7–S9, and Table S1). All these species have a BE equal or lower than the Ir^{IV} bulk component for the Ir 4f, and most present little or no t_{2g} (*ca.* 529 eV) resonance in the O K-edge. The pDOS shows that for μ_2-O formation on Ir^{III} a loss in the O 2p intensity is expected (Fig. S9†), opposite to the observed gain in intensity observed experimentally (Fig. 3c and d) and predicted for μ_2-O on $Ir^{IV+\delta}$ (Fig. 3a and b). The combined observed changes in Ir 4f, O K-edge and VB for the rutile type IrO_2 under O_2 are entirely consistent solely with the computed Ir 4f and O K-edge spectra and pDOS for μ_2-O on $Ir^{IV+\delta}$, thus supporting the assignment of the formed species to μ_2-O formed in the absence of Ir^{III}.

As noted above, the computed surface phase diagram (Fig. 1) predicts μ_1-OH remains stable across the entire range of oxygen chemical potentials accessible under NAP-XPS conditions and the experiments show no sign of the 528 eV resonance associated with the formation of μ_1-O (ref. 10 and 23) (see Fig. S2†) argued to be active in electrochemical water oxidation. Moreover, the VB measurements also show no sign of the formation of μ_1-O (see Fig. S10†). Thus, we can then expect that μ_2-O can be formed by thermal oxidation in addition to electrochemical oxidation, whereas μ_1-O formation requires more oxidizing conditions than those accessible in this work, in good agreement with the computed surface phase diagram.

To verify the μ_2-O formed on rutile-type IrO_2 in the absence of Ir^{III} has the chemical behavior associated with O^{I-} we can also explore its reactivity with CO. The μ_2-O species linked to the high OER activity on amorphous IrO_x have been shown to have an electrophilic nature and to be active in room temperature CO oxidation,[17,50] without any pre-treatment. Moreover, iridium oxyhydroxides with high concentration of μ_2-O species were shown to lose OER activity after partial titration of the μ_2-O species with CO, showing

μ_2-O plays a prominent role in the OER performances of iridium based (oxyhydr)oxides,[50] In contrast, rutile-type IrO_2 without any pre-treatment is not active in CO oxidation at room temperature.[17] With this in mind, we turn to testing the chemistry of the thermally produced species on rutile-type IrO_2.

After producing μ_2-O on rutile-type IrO_2 through O_2 treatment at 573 K, the sample was cooled to room temperature and placed under vacuum. It was then exposed to 0.25 mbar CO at room temperature and the O K-edge was monitored. Upon CO exposure CO_2 was produced (Fig. 4a). At the same time, the resonance developed at *ca.* 529 eV at the O-K edge for the O_2-treated rutile-type IrO_2 can be seen to disappear, indicating the loss of μ_2-O (Fig. 4b and S11†). The Ir 4f spectrum can be seen to lose the previously gained high-energy broadening (Fig. 4c) and a similar difference-spectrum (from that in Fig. 2a) is obtained when comparing the rutile-type IrO_2 treated under O_2 and the same sample

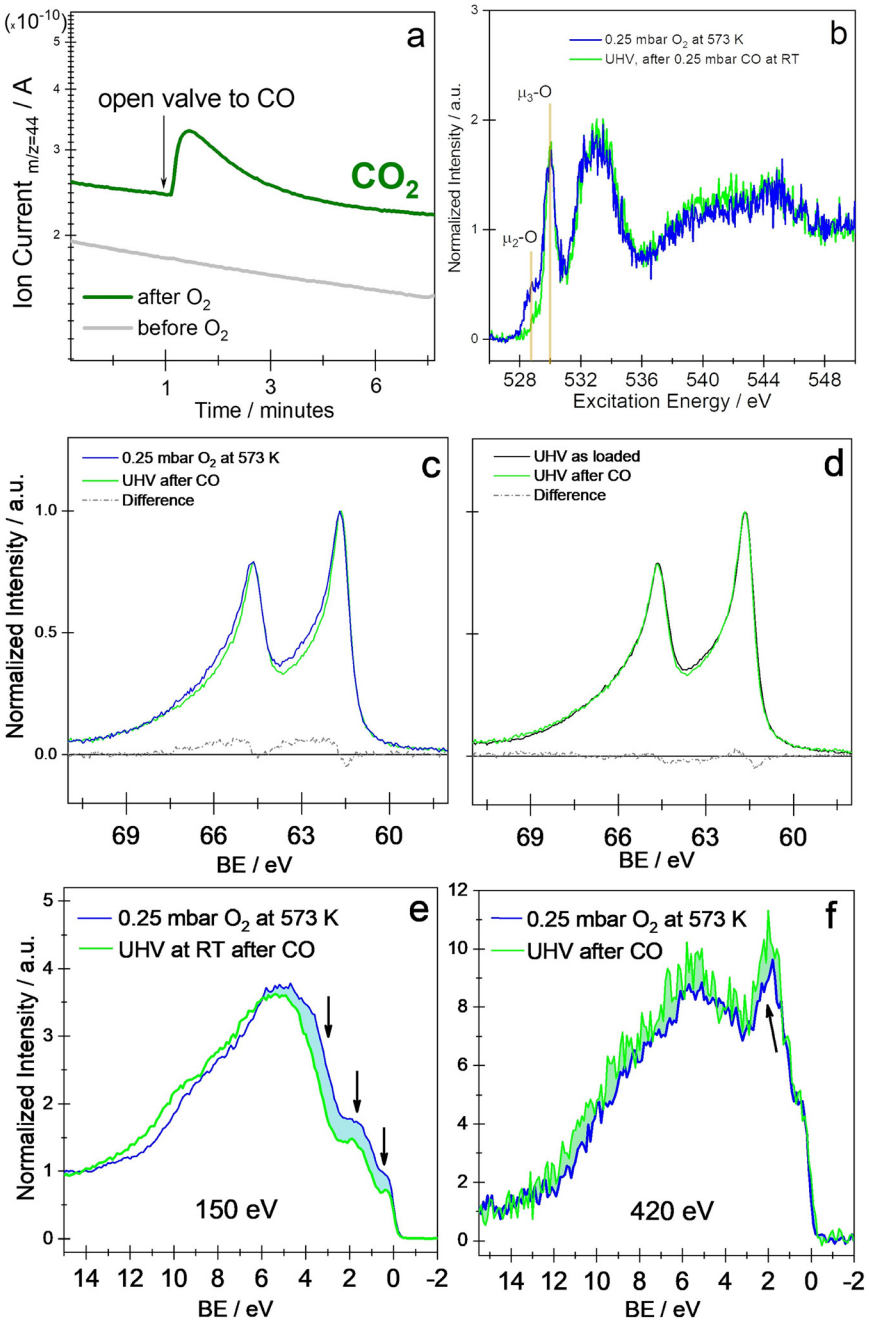

Fig. 4 Here: (a) CO_2 signal (m/z = 44) from on-line QMS for rutile-type IrO_2 exposed to 0.25 mbar of CO at RT, before and after O_2 treatment at 573 K. (b) O K-edge of rutile-type IrO_2 under 0.25 mbar O_2 at 573 K and in UHV after CO at RT. (c and d) Ir 4f of rutile-type IrO_2 under 0.25 mbar O_2 at 573 K, in UHV after CO at RT and in UHV as loaded. The difference spectra are also shown. (e and f) VB of rutile-type IrO_2 measured at 150 eV (e) and 420 eV (f) under 0.25 mbar O_2 at 573 K and in UHV after CO at RT.

after exposure to CO (Fig. 4c). A difference spectrum between the Ir 4f spectra of the rutile-type IrO_2 before the O_2 treatment and after exposure to CO confirms that the spectrum of the rutile-type IrO_2 after CO exposure is the same as before the O_2 treatment (Fig. 4d). That is, the μ_2-O formed on $Ir^{IV+\delta}$ by the thermal oxygen treatment was titrated by CO. Moreover, the VB (Fig. 4e) measured at 150 eV (sensitive to the O 2p) shows the loss of intensity related to the μ_2-O species (compare Fig. 4e to 3c), and the VB (Fig. 4f) measured at 420 eV (dominated by the Ir 5d) shows a slight increase of intensity related to the loss of $Ir^{IV+\delta}$ (compare Fig. 4f to 3b). The changes are seen to be again (although small) reproducible (Fig. S12 and S13†). With all the above we confirm that the species produced on rutile-type IrO_2 by (mild) thermal oxidation has the same chemical nature as the O^{I-} present on/in highly active amorphous iridium oxides. Thus, we have successfully produced electron deficient (electrophilic) oxygen species on rutile-type IrO_2 by thermal oxidation of μ_2-OH species (accompanied by oxidation of Ir^{IV} to $Ir^{IV+\delta}$) without the need of Ir^{III} species. Depth profiling (Fig. S14†) reveals that the species produced under the O_2 treatment are located in the (near) surface of the IrO_2. This is in agreement with μ_2-OH deprotonation on rutile-type IrO_2 under OER occurring mainly on the surface,[10] rendering only low concentrations of O^{I-} on the less active rutile-type IrO_2.

To address why μ_2-O species have not been spectroscopically observed on rutile-type IrO_2 at room temperature previously we return to *ab initio* thermodynamics. Even at O_2 partial pressure as high as *ca.* 210 mbar and H_2O partial pressure as low as 10^{-12} mbar, μ_2-OH is the thermodynamically preferred species at room temperature (Fig. S15†). This means that when rutile-type IrO_2 is exposed to any water traces, or other hydrogen sources, μ_2-OH will form at room temperature. In our experiments we found that during the cooling ramp after the O_2 treatment of the rutile-type IrO_2, the resonance at 529 eV (which corresponds to μ_2-O) decreased with time (even under O_2 which contains a maximum of 0.5 ppm H_2O, *i.e.* on the order of 10^{-7} mbar H_2O in the 0.25 mbar O_2). With the chosen protocol (see Methodology section) the μ_2-O species remained on the surface long enough to probe their chemistry by exposing the sample to CO, as we have shown above.

This observation and the *ab initio* atomistic thermodynamics results agree with the strong dissociative adsorption of H_2O (ref. 27 and 52) and the previously observed fast protonation of oxygen surface species under UHV by background H_2 (ref. 30) reported on IrO_2 surfaces. Thus, any rutile-type IrO_2 in the presence of small ($\geq$0.5 ppm) amounts of water will have a hydroxylated surface with protonated μ_2-OH and μ_1-OH species. And while we have developed a protocol to prepare μ_2-O *via* thermal oxidation, the stronger O–H bond of μ_1-OH makes preparation of μ_1-O more challenging and we were unable to produce this species under gas-phase NAP-XPS conditions. Experiments as described here verify the reactive oxyl species is only formed under higher oxygen chemical potential.

Under these controlled preparation conditions, it becomes possible to address an unresolved aspect of electron deficient oxygen or O^{I-}. The electron deficient μ_2-O species has been described in hydrated amorphous IrO_x to be formed in a matrix of mixed $Ir^{III/IV}$ oxide, though no direct link between Ir^{III} and O^{I-} was established.[15,16] And although Ir^{III} might be present under OER conditions, and a wide variety of defects and iridium oxidation states present in amorphous materials may facilitate lattice oxidation and Ir dissolution,[53–55] here we have shown that under O_2 at 573 K the electron deficient μ_2-O species appearing on crystalline IrO_2 are formed on $Ir^{IV+\delta}$ without the need for Ir^{III}. It thus appears that the Ir^{III} present in amorphous IrO_x is unrelated to O^{I-}, which has important consequences for Ir-based OER catalysts as Ir^{III} is unstable.[19]

Our work shows increasing the O^{I-} coverage through doping[11] or variation in local atomic structure[20,21] need not introduce Ir^{III}. This may then offer a route to higher-performance stable OER catalysts. Here, designing complex oxides with stable basic-coordination sites acting as proton-acceptors next to the reactive Ir species could be a good approach to better OER catalysts.

Conclusions

Using *ab initio* atomistic thermodynamics, we have predicted the surface phase diagram of rutile-type IrO_2 under gas phase O_2 and trace amounts of water. We computed the spectroscopic properties of these surface phases and confirmed the *ab initio* atomistic thermodynamics predictions by means of XPS and XAS. We found mild thermal oxidation of rutile-IrO_2 is sufficient to form an electron deficient O-species, μ_2-O bound to $Ir^{IV+\delta}$ sites. This species is not present at room temperature over rutile-type IrO_2 due to the high hydrogen affinity of μ_2-O, which becomes hydroxylated even at extremely low (10^{-12} mbar) water (and high O_2) partial pressure. With CO titration experiments we confirmed the chemical nature of the produced species, allowing us to show μ_2-O has the same spectroscopic and chemical properties associated with the O^{I-} species whose coverage is related to OER activity of Ir-based materials. By preparing this O^{I-} under controlled conditions, however, we were able to show its presence does not require Ir^{III}, which could offer a route to higher-performance stable OER catalysts.

Conflicts of interest

There are no conflicts to declare.

Acknowledgements

We thank the Helmholtz-Zentrum Berlin für Materialien und Energie GmbH BESSYII synchrotron light source for providing support of the *in situ* electron spectroscopy activities of the

Fritz Haber Institute der Max Planck Gesellschaft, and we thanks the Max-Planck Gesellschaft for generous founding. TJ acknowledges support from the Laboratory Directed Research and Development program of Los Alamos National Laboratory under project number 20240061 DR. Open Access funding provided by the Max Planck Society.

References

1 N. Danilovic, R. Subbaraman, K. C. Chang, S. H. Chang, Y. J. J. Kang, J. Snyder, A. P. Paulikas, D. Strmcnik, Y. T. Kim, D. Myers, V. R. Stamenkovic and N. M. Markovic, *J. Phys. Chem. Lett.*, 2014, **5**, 2474–2478.

2 S. Cherevko, S. Geiger, O. Kasian, N. Kulyk, J. P. Grote, A. Savan, B. R. Shrestha, S. Merzlikin, B. Breitbach, A. Ludwig and K. J. J. Mayrhofer, *Catal. Today*, 2016, **262**, 170–180.

3 M. Carmo, D. L. Fritz, J. Merge and D. Stolten, *Int. J. Hydrogen Energy*, 2013, **38**, 4901–4934.

4 M. Schalenbach, G. Tjarks, M. Carmo, W. Lueke, M. Mueller and D. Stolten, *J. Electrochem. Soc.*, 2016, **163**, F3197–F3208.

5 T. Naito, T. Shinagawa, T. Nishimoto and K. Takanabe, *Inorg. Chem. Front.*, 2021, **8**, 2900–2917.

6 Z. J. Chen, X. G. Duan, W. Wei, S. B. Wang and B. J. Ni, *Nano Energy*, 2020, **78**, 105270.

7 C. Wang, F. F. Lan, Z. F. He, X. F. Xie, Y. H. Zhao, H. Hou, L. Guo, V. Murugadoss, H. Liu, Q. Shao, Q. Gao, T. Ding, R. B. Wei and Z. H. Guo, *ChemSusChem*, 2019, **12**, 1576–1590.

8 H. Jang and J. Lee, *J. Energy Chem.*, 2020, **46**, 152–172.

9 H. Wu, Y. Wang, Z. Shi, X. Wang, J. Yang, M. Xiao, J. Ge, W. Xing and C. Liu, *J. Mater. Chem. A*, 2022, **10**, 13170–13189.

10 R. V. Mom, L. J. Falling, O. Kasian, G. Algara-Siller, D. Teschner, R. H. Crabtree, A. Knop-Gericke, K. J. J. Mayrhofer, J.-J. Velasco-Vélez and T. E. Jones, *ACS Catal.*, 2022, **12**, 5174–5184.

11 H. N. Nong, T. Reier, H. S. Oh, M. Gliech, P. Paciok, T. H. T. Vu, D. Teschner, M. Heggen, V. Petkov, R. Schlogl, T. Jones and P. Strasser, *Nat. Catal.*, 2018, **1**, 841–851.

12 V. Pfeifer, T. E. Jones, J. J. Velasco Vélez, R. Arrigo, S. Piccinin, M. Hävecker, A. Knop-Gericke and R. Schlögl, *Chem. Sci.*, 2017, **8**, 2143–2149.

13 V. A. Saveleva, L. Wang, D. Teschner, T. Jones, A. S. Gago, K. A. Friedrich, S. Zafeiratos, R. Schlogl and E. R. Savinova, *J. Phys. Chem. Lett.*, 2018, **9**, 3154–3160.

14 H. N. Nong, L. J. Falling, A. Bergmann, M. Klingenhof, H. P. Tran, C. Spori, R. Mom, J. Timoshenko, G. Zichittella, A. Knop-Gericke, S. Piccinin, J. Perez-Ramirez, B. R. Cuenya, R. Schlogl, P. Strasser, D. Teschner and T. E. Jones, *Nature*, 2021, **589**, E8.

15 V. Pfeifer, T. E. Jones, J. J. V. Velez, C. Massue, M. T. Greiner, R. Arrigo, D. Teschner, F. Girgsdies, M. Scherzer, J. Allan, M. Hashagen, G. Weinberg, S. Piccinin, M. Havecker, A. Knop-Gericke and R. Schlogl, *Phys. Chem. Chem. Phys.*, 2016, **18**, 2292–2296.

16 V. Pfeifer, T. E. Jones, J. J. V. Velez, C. Massue, R. Arrigo, D. Teschner, F. Girgsdies, M. Scherzer, M. T. Greiner, J. Allan, M. Hashagen, G. Weinberg, S. Piccinin, M. Havecker, A. Knop-Gericke and R. Schlogl, *Surf. Interface Anal.*, 2016, **48**, 261–273.

17 V. Pfeifer, T. E. Jones, S. Wrabetz, C. Massue, J. J. V. Velez, R. Arrigo, M. Scherzer, S. Piccinin, M. Havecker, A. Knop-Gericke and R. Schlogl, *Chem. Sci.*, 2016, **7**, 6791–6795.

18 J. J. Velasco-Velez, E. A. Carbonio, C. H. Chuang, C. J. Hsu, J. F. Lee, R. Arrigo, M. Havecker, R. Z. Wang, M. Plodinec, F. R. Wang, A. Centeno, A. Zurutuza, L. J. Falling, R. V. Mom, S. Hofmann, R. Schlogl, A. Knop-Gericke and T. E. Jones, *J. Am. Chem. Soc.*, 2021, **143**, 12524–12534.

19 O. Kasian, J. P. Grote, S. Geiger, S. Cherevko and K. J. J. Mayrhofer, *Angew. Chem., Int. Ed.*, 2018, **57**, 2488–2491.

20 E. Willinger, C. Massue, R. Schlogl and M. G. Willinger, *J. Am. Chem. Soc.*, 2017, **139**, 12093–12101.

21 M. Elmaalouf, M. Odziomek, S. Duran, M. Gayrard, M. Bahri, C. Tard, A. Zitolo, B. Lassalle-Kaiser, J. Y. Piquemal, O. Ersen, C. Boissiere, C. Sanchez, M. Giraud, M. Faustini and J. Peron, *Nat. Commun.*, 2021, **12**, 3935.

22 J. J. Velasco-Velez, T. E. Jones, V. Streibel, M. Havecker, C. H. Chuang, L. Frevel, M. Plodinec, A. Centeno, A. Zurutuza, R. Wang, R. Arrigo, R. Mom, S. Hofmann, R. Schlogl and A. Knop-Gericke, *Surf. Sci.*, 2019, **681**, 1–8.

23 L. J. Frevel, R. Mom, J.-J. Velasco-Vélez, M. Plodinec, A. Knop-Gericke, R. Schlögl and T. E. Jones, *J. Phys. Chem. C*, 2019, **123**, 9146–9152.

24 T. Reier, Z. Pawolek, S. Cherevko, M. Bruns, T. Jones, D. Teschner, S. Selve, A. Bergmann, H. N. Nong, R. Schlogl, K. J. J. Mayrhofer and P. Strasser, *J. Am. Chem. Soc.*, 2015, **137**, 13031–13040.

25 P. Strasser, *Acc. Chem. Res.*, 2016, **49**, 2658–2668.

26 H. N. Nong, H. P. Tran, C. Spöri, M. Klingenhof, L. Frevel, T. E. Jones, T. Cottre, B. Kaiser, W. Jaegermann, R. Schlögl, D. Teschner and P. Strasser, *Z. Phys. Chem.*, 2020, **234**, 787–812.

27 D. Gonzalez, J. Heras-Domingo, S. Pantaleone, A. Rimola, L. Rodriguez-Santiago, X. Solans-Monfort and M. Sodupe, *ACS Omega*, 2019, **4**, 2989–2999.

28 T. Li, M. Kim, Z. Liang, A. Asthagiri and J. F. Weaver, *Top. Catal.*, 2018, **61**, 397–411.

29 M. J. S. Abb, T. Weber, D. Langsdorf, V. Koller, S. M. Gericke, S. Pfaff, M. Busch, J. Zetterberg, A. Preobrajenski, H. Grönbeck, E. Lundgren and H. Over, *J. Phys. Chem. C*, 2020, **124**, 15324–15336.

30 R. Martin, M. Kim, C. J. Lee, V. Mehar, S. Albertin, U. Hejral, L. R. Merte, E. Lundgren, A. Asthagiri and J. F. Weaver, *J. Phys. Chem. Lett.*, 2020, **11**, 7184–7189.

31 K. J. S. Sawhney, F. Senf, M. Scheer, F. Schäfers, J. Bahrdt, A. Gaupp and W. Gudat, *Nucl. Instrum. Methods Phys. Res., Sect. A*, 1997, **390**, 395–402.

32 S. Tanuma, C. J. Powell and D. R. Penn, *Surf. Interface Anal.*, 1994, **21**, 165–176.

33 IrO2 Crystal Structure: Datasheet from "*PAULING FILE Multinaries Edition – 2012*" in SpringerMaterials (**https://materials.springer.com/isp/crystallographic/docs/sd_0457154**); Springer-Verlag Berlin Heidelberg & Material Phases Data System (MPDS), Switzerland & National Institute for Materials Science (NIMS), Japan.

34 P. Giannozzi, S. Baroni, N. Bonini, M. Calandra, R. Car, C. Cavazzoni, D. Ceresoli, G. L. Chiarotti, M. Cococcioni, I. Dabo, A. Dal Corso, S. de Gironcoli, S. Fabris, G. Fratesi, R. Gebauer, U. Gerstmann, C. Gougoussis, A. Kokalj, M. Lazzeri, L. Martin-Samos, N. Marzari, F. Mauri, R. Mazzarello, S. Paolini, A. Pasquarello, L. Paulatto, C. Sbraccia, S. Scandolo, G. Sclauzero, A. P. Seitsonen, A. Smogunov, P. Umari and R. M. Wentzcovitch, *J. Phys.: Condens. Matter*, 2009, **21**, 395502.

35 P. Giannozzi, O. Andreussi, T. Brumme, O. Bunau, M. B. Nardelli, M. Calandra, R. Car, C. Cavazzoni, D. Ceresoli, M. Cococcioni, N. Colonna, I. Carnimeo, A. Dal Corso, S. de Gironcoli, P. Delugas, R. A. DiStasio, A. Ferretti, A. Floris, G. Fratesi, G. Fugallo, R. Gebauer, U. Gerstmann, F. Giustino, T. Gorni, J. Jia, M. Kawamura, H. Y. Ko, A. Kokalj, E. Kucukbenli, M. Lazzeri, M. Marsili, N. Marzari, F. Mauri, N. L. Nguyen, H. V. Nguyen, A. Otero-de-la-Roza, L. Paulatto, S. Ponce, D. Rocca, R. Sabatini, B. Santra, M. Schlipf, A. P. Seitsonen, A. Smogunov, I. Timrov, T. Thonhauser, P. Umari, N. Vast, X. Wu and S. Baroni, *J. Phys.: Condens. Matter*, 2017, **29**, 465901.

36 J. P. Perdew, K. Burke and M. Ernzerhof, *Phys. Rev. Lett.*, 1996, **77**, 3865–3868.

37 A. Dal Corso, *Comput. Mater. Sci.*, 2014, **95**, 337–350.

38 G. Novell-Leruth, G. Carchini and N. López, *J. Chem. Phys.*, 2013, **138**, 194706.

39 J. Rossmeisl, Z. W. Qu, H. Zhu, G. J. Kroes and J. K. Norskov, *J. Electroanal. Chem.*, 2007, **607**, 83–89.

40 T. D. Nguyen, G. G. Scherer and Z. C. J. Xu, *Electrocatalysis*, 2016, **7**, 420–427.

41 N. Marzari, D. Vanderbilt, A. De Vita and M. C. Payne, *Phys. Rev. Lett.*, 1999, **82**, 3296–3299.

42 C. Gougoussis, M. Calandra, A. P. Seitsonen and F. Mauri, *Phys. Rev. B: Condens. Matter Mater. Phys.*, 2009, **80**, 075102.

43 E. Pehlke and M. Scheffler, *Phys. Rev. Lett.*, 1993, **71**, 2338–2341.

44 T. E. Jones, T. C. R. Rocha, A. Knop-Gericke, C. Stampfl, R. Schlogl and S. Piccinin, *Phys. Chem. Chem. Phys.*, 2015, **17**, 9288–9312.

45 K. Reuter and M. Scheffler, *Phys. Rev. B: Condens. Matter Mater. Phys.*, 2002, **65**, 035406.

46 C. F. S. Codeco, A. Y. Klyushin, E. A. Carbonio, A. Knop-Gericke, R. Schlogl, T. Jones and T. C. R. Rocha, *Phys. Chem. Chem. Phys.*, 2022, **24**, 8832–8838.

47 E. H. P. Cordfunke, *Thermochim. Acta*, 1981, **50**, 177–185.

48 M. W. Chase Jr., NIST-JANAF thermochemical tables, *J. Phys. Chem. Ref. Data, Monogr.*, 1998, DOI: **10.18434/T42S31**.

49 J. J. V. Velez, D. Bernsmeier, T. E. Jones, P. Zeller, E. Carbonio, C. H. Chuang, L. J. Falling, V. Streibel, R. V. Mom, A. Hammud, M. Havecker, R. Arrigo, E. Stotz, T. Lunkenbein, A. Knop-Gericke, R. Krahnert and R. Schlogl, *Faraday Discuss.*, 2022, **236**, 103–125.

50 C. Massue, V. Pfeifer, M. van Gastel, J. Noack, G. Algara-Siller, S. Cap and R. Schlogl, *ChemSusChem*, 2017, **10**, 4786–4798.

51 J. J. Yeh and I. Lindau, *At. Data Nucl. Data Tables*, 1985, **32**, 1–155.

52 D. González, M. Sodupe, L. Rodríguez-Santiago and X. Solans-Monfort, *Nanoscale*, 2021, **13**, 14480–14489.

53 A. Loncar, D. Escalera-López, S. Cherevko and N. Hodnik, *Angew. Chem., Int. Ed.*, 2022, **61**, e202114437.

54 A. Zagalskaya and V. Alexandrov, *J. Phys. Chem. Lett.*, 2020, **11**, 2695–2700.

55 L. A. She, G. Q. Zhao, T. Y. Ma, J. Chen, W. P. Sun and H. G. Pan, *Adv. Funct. Mater.*, 2022, **32**, 2108465.

